small
NANO MICRO
www.small-journal.com

Chiral Shell Core–Satellite Nanostructures for Ultrasensitive Detection of Mycotoxin

Jiarong Cai, Changlong Hao, Maozhong Sun, Wei Ma, Chuanlai Xu, and Hua Kuang**

Herein, the design of a DNA-based chiral biosensor is described utilizing the self-assembly of shell core–gold (Au) satellite nanostructures for the detection of mycotoxin, ochratoxin A (OTA). The assembly of core–satellite nanostructures based on OTA-aptamer binding exhibits a strong chiral signal with an intense circular dichroism (CD) peak. The integrity of the assembly of core–satellite nanostructures is limited to some extent in the presence of different levels of OTA. Correspondingly, the chiral intensity of assembly is weakened with increasing OTA concentrations, allowing quantitative determination of the target. The developed chiral sensor shows an excellent linear relationship between the CD signal and concentrations of OTA in the range of 0.1–5 pg mL^{-1} with a limit of detection as low as 0.037 pg mL^{-1}. The effectiveness of the biosensor in a sample of red wine is verified and a good recovery rate is obtained. These results suggest that the strategy has great potential for practical application.

1. Introduction

Ochratoxin A (OTA) is a foodborne mycotoxin that exhibits potential carcinogenicity, immunosuppression, and hepatoxicity, and it has been the focus of food safety testing.[1–3] The mycotoxins are produced in response to the improper storage of foodstuffs and contaminates food, such as cacao, cereals, fruits, dried fruits, beer, and wine.[4,5] Traditional analytical methods, for example, high-performance liquid chromatography,[6] gas chromatography combined with mass spectrometry,[7] and the enzyme-linked immunosorbent assay (ELISA),[8–10] require sophisticated instruments, complex sample preparation steps, and trained staff.[11,12] Although exceptional progress has been achieved in electrochemical[13] and polymerase chain reaction methods,[14,15] the complex preprocessing steps and severe matrix disturbances involved largely limit the sensitivity of OTA detection in actual samples. To effectively quantify the occurrence of OTA in food contaminated with low levels of this mycotoxin, the development of a practical method for OTA detection is desirable.

Self-assembled nanosuperstructures have become a focus of attention due to their delicate, innovative, structurally well-defined, and unique optical properties.[16,17] Several studies have reported the synthesis,[18,19] mechanisms,[20,21] catalytic,[22] and detection[23] properties of self-assembled structures. At present, the fluorescence characteristics of simple self-assembled nanostructures, such as nanoclusters[24] and magnetic probes,[25,26] are used for biotoxin testing. However, the stability, dispersibility, and biocompatibility of fluorescent dyes and granules limit their practical application.[27,28] The surface-enhanced Raman scattering (SERS) properties of nanomaterials, such as nanostars,[29] core–shell nanocubes,[30,31] and nanocapsules[32] are used as signals for biosensors, also. However, signal sensitivity still needs to be improved.

In our previous work, we found that, due to the dipole–dipole interaction between particles during the assembly of self-assembled nanosuperstructures, a strong chiral signal is produced at the position of the surface plasmon resonance peak.[33] Already described chiral superstructures include nanotweezers[34] and nanotubes.[35] The features of the assembly of such structures can be used for high-sensitivity detection of biological samples, with only minor interference from the matrix. Up to now, simple self-assembled nanostructures, such as dimers,[36,37] pyramids,[38] and propeller-like nanoscale assemblies[39] have been used in highly sensitive biological assays. However, these relatively simple self-assembled nanostructures have weak circular dichroism (CD) peaks.[40,41] In order to improve the sensitivity of the detection, a superstructure with a high CD signal is necessary to be fabricated.

Here, we have developed a DNA-based self-assembled core–satellite superstructure comprised of shell (24.8 nm ± 4.2 nm) and gold (Au) NPs (15 nm ± 3 nm) as a chiral biosensor to achieve rapid and highly sensitive detection of OTA. As illustrated in **Scheme 1**, shell and Au nanoparticle (NP) surfaces were coupled to aptamers of OTA and their complementary

J. Cai, Dr. C. Hao, Dr. M. Sun, Dr. W. Ma, Prof. C. Xu, Prof. H. Kuang
State Key Laboratory of Food Science and Technology
Jiangnan University
Wuxi, Jiangsu 214122, P. R. China
E-mail: mawei209@126.com; kuangh@jiangnan.edu.cn
J. Cai, Dr. C. Hao, Dr. M. Sun, Dr. W. Ma, Prof. C. Xu, Prof. H. Kuang
International Joint Research Laboratory for Biointerface
and Biodetection, and School of Food Science and Technology
Jiangnan University
Wuxi, Jiangsu 214122, P. R. China
J. Cai, Dr. C. Hao, Dr. M. Sun, Dr. W. Ma, Prof. C. Xu, Prof. H. Kuang
Collaborative Innovation Center of Food Safety and Quality Control in
Jiangsu Province
Jiangnan University
Wuxi, Jiangsu 214122, P. R. China
The ORCID identification number(s) for the author(s) of this article can be found under https://doi.org/10.1002/smll.201703931.

DOI: 10.1002/smll.201703931

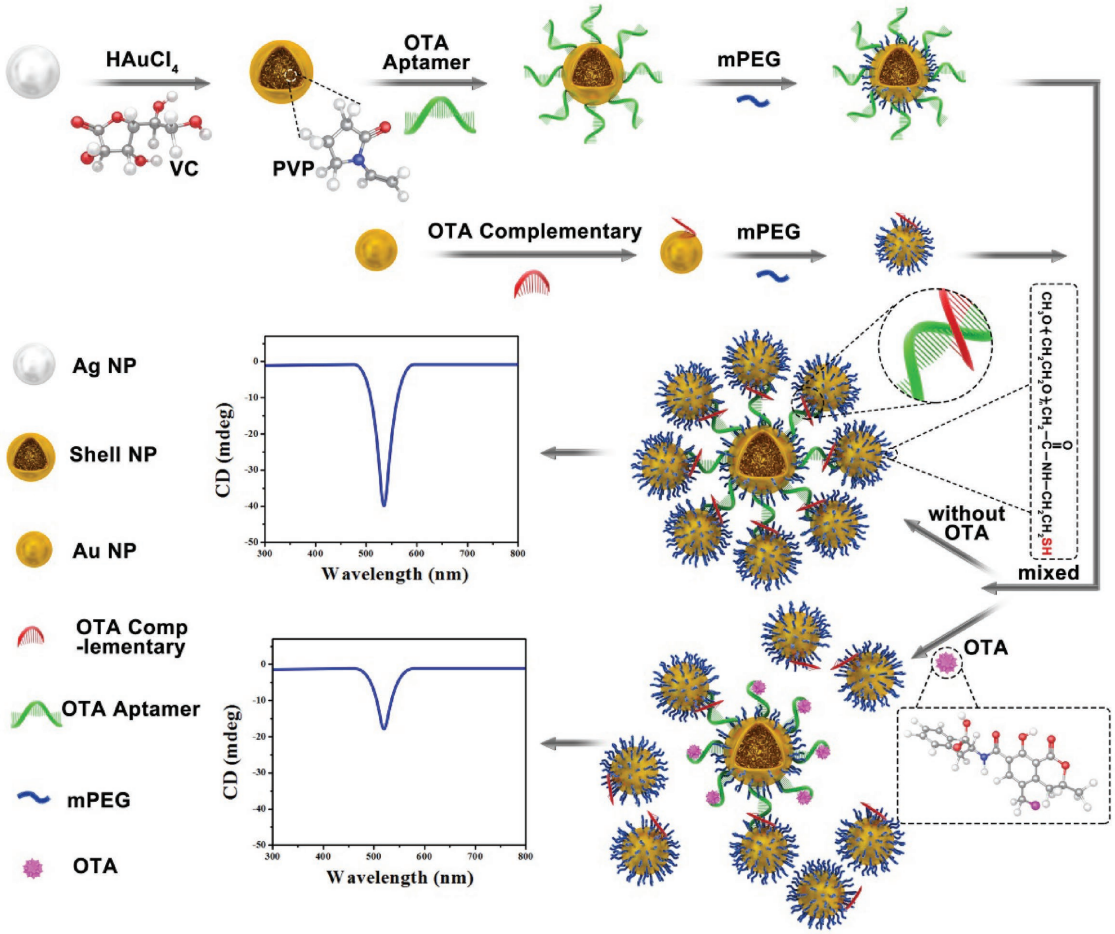

Scheme 1. Schematic representation of OTA detection based on chiral signal of shell core–Au satellite superstructures.

sequences, respectively. In the absence of OTA, the high-yielding shell core–Au satellite structures elicited a strong chiral signal. In the presence of OTA, meanwhile, the coupling degree of the structure decreased with increasing OTA concentration and the chiral signal was weakened.

2. Results and Discussion

2.1. Structural and Optical Characterization of Shell Core–Au Satellite

The Au NPs were synthesized using sodium citrate reduction. As shown in Figure S1A (Supporting Information), the pellets had a good morphology and were evenly dispersed in the aqueous phase. The particle sizes of Au NPs and single-stranded DNA-modified Au NPs were characterized by dynamic light scattering (DLS) (Figure S1B, Supporting Information). The result shows that the Au NPs modified with DNA were larger than the naked Au NPs, indicating that DNA was successfully incorporated onto the surface of Au NPs. The preparation of the shell NPs, meanwhile, consisted of two steps. First, an Au–Ag alloyed hollow sphere was formed via a galvanic replacement reaction between Ag NPs and $HAuCl_4$ as the $AuCl_4$/Au redox pair possesses a higher standard reduction potential than the Ag^+/Ag redox pair,[42] and then a thin layer of Au was deposited onto the surface of the hollow sphere by reducing $HAuCl_4$ with ascorbic acid. Figure S2A (Supporting Information) shows transmission electron microscopy (TEM) images obtained from a sample of shell NPs. It can be observed that the particles are hollow and have a thin layer of gold on their outer layers. The DLS data (Figure S2B, Supporting Information) showed that the oligonucleotides were successfully incorporated onto the surface of shell NPs. We counted the size of the shell NPs in 100 TEM images and found that shell NPs vary in size, with a statistical result of 24.8 nm ± 4.2 nm, which is inconsistent with a wide range of DLS data. We considered the surface roughness of the shell NPs, which is not the standard sphere, as the reason for the wider size distribution. The diameter of the core–satellite structures was measured (Figure S3, Supporting Information), which revealed that the size of the particles was about 80 nm. The DLS data showed that a small amount of unsuccessfully assembled NPs was to be found in the satellite solution. The size of the satellite structures was significantly larger than the size of the shell or Au NPs, indicating successful assembly. We also provided TEM images of a mixture of modified and unmodified complementary DNA shell and Au NPs for 12 h (Figure S4, Supporting Information). This

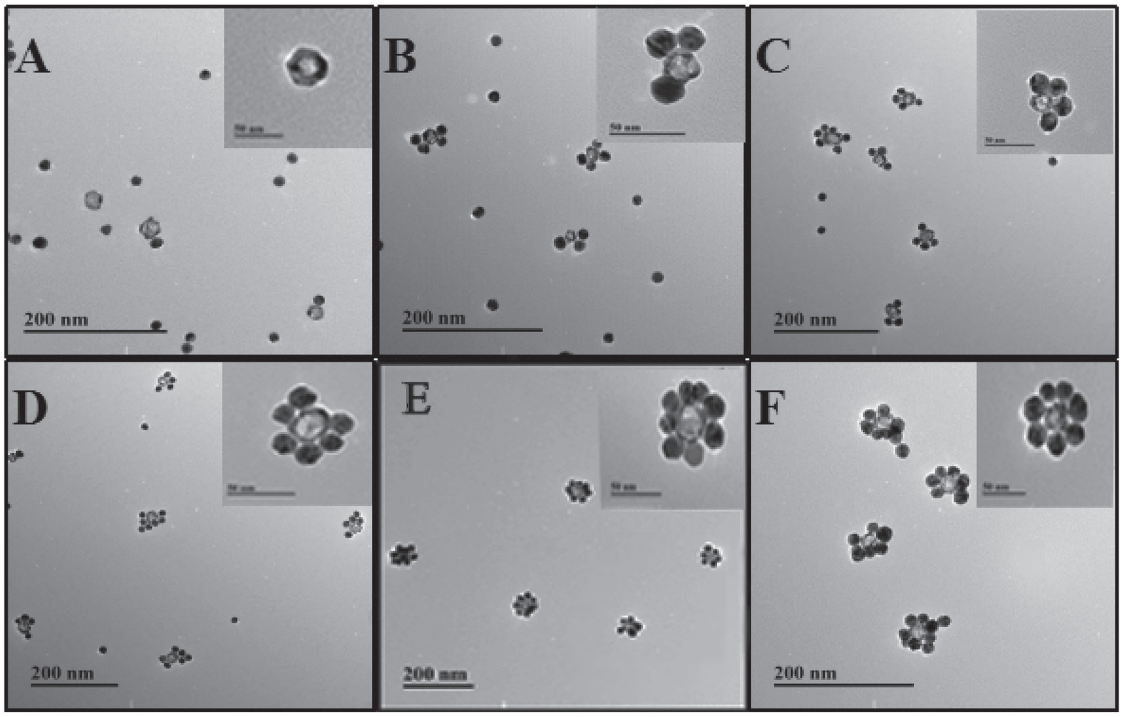

Figure 1. Representative TEM images of shell core–Au satellite superstructures at different incubation times, A) 0.5 h, B) 3 h, C) 6 h, D) 9 h, E) 12 h, and F) 15 h. The insets show TEM images of Individual representative nanostructures at a higher magnification (scale bar was 50 nm).

result demonstrates that the DNA successfully bound to the NP surface, consistent with the results of the DLS.

The self-assembly of the core–satellite structures was carried out by mixing the prepared DNA-modified shell and Au NPs at a molar ratio of 1:8. The degree of assembly varied with the incubation times as shown in **Figure 1**. With increasing time, the number of Au NPs coupled to the surface of a single shell NP increased gradually and became saturated after 12 h. No significant difference was observed between 12 and 15 h, indicating that the particles were fully coupled after 12 h. In view of this, we used 12 h as the incubation time. Representative TEM image of high-yield shell core–Au satellite superstructures is shown in Figure S5 (Supporting Information). The changes in optical properties after different incubation times were determined (**Figure 2**). During 0–15 h of incubation, the position of the CD peak did not change, but the intensity of the CD signal gradually increased and then stabilized. We can conclude that the intensity of the bands produced depends mainly on the number of Au NPs coupled to the shell NPs. The higher the number of Au NPs adsorbed on the surface of the shell NPs, the stronger the CD signal. This conclusion can explain the observation that the CD signals no longer changed after 12 h, since the surface of the shell NPs was completely covered by Au NPs after 12 h, the CD signal no longer increased. There was no significant difference between UV–vis spectra from different time points. It's true that aggregation of NPs can produce redshift absorption peak, and the stronger the force between the NPs, the more obvious redshift. Whereas no significant changes in the UV–vis spectra were observed, we believe this is due to the existence of a certain distance between the DNA-coupled Au and shell NPs that does not result in an efficient absorption spectrum shift. Conversely, a CD signal can produce a significant change in signal intensity with no change in absorption. This is due to the fact that long-range coupling can produce chiral signals, which is consistent with our previous findings.[43,44] The surface electrical field distribution maps for shell NP, Au NP, and core–satellite assembly are shown in Figure 2C–E. With the integration of a gap in single-shell NPs (*E*-field 11 V m^{-1}), the surrounded Au NPs on shell NPs (shell–satellite assemblies) gave rise to the strongest *E*-field of 29 V m^{-1}. The electric field for NPs (15 nm) assembled around Au NPs (25 nm) was 17 V m^{-1}, which was due to an enhancement of the electric field by Au NP–Au NP gap junctions. The combination of core–shell Au NPs (integrated gaps) and core–satellite assemblies (Au NPs–Au NPs junctions) gave rise to the highest hot spot enhancement. After 12 h of incubation, the obtained complete core–satellite superstructure had a high yield which reached about 85% (statistical analysis of up to 100 TEM images). Only a small number of Au NPs scattered in the solution. Statistical analysis of the percentage of Au NPs surrounding the shell NPs at different incubation times is shown in **Figure 3**. The production statistics show that the assembly of the core–satellite structure is a dynamic process, and that, as indicated above, 12 h are necessary for the process of dynamic assembly to reach saturation point.

CD and UV–vis spectra were determined for assembled shell core–Au satellite superstructures and other constituent materials (**Figure 4**). It is worth noting that only the assembled core–satellite structure had a chiral signal. We recently discovered that there is a small dihedral angle between the core

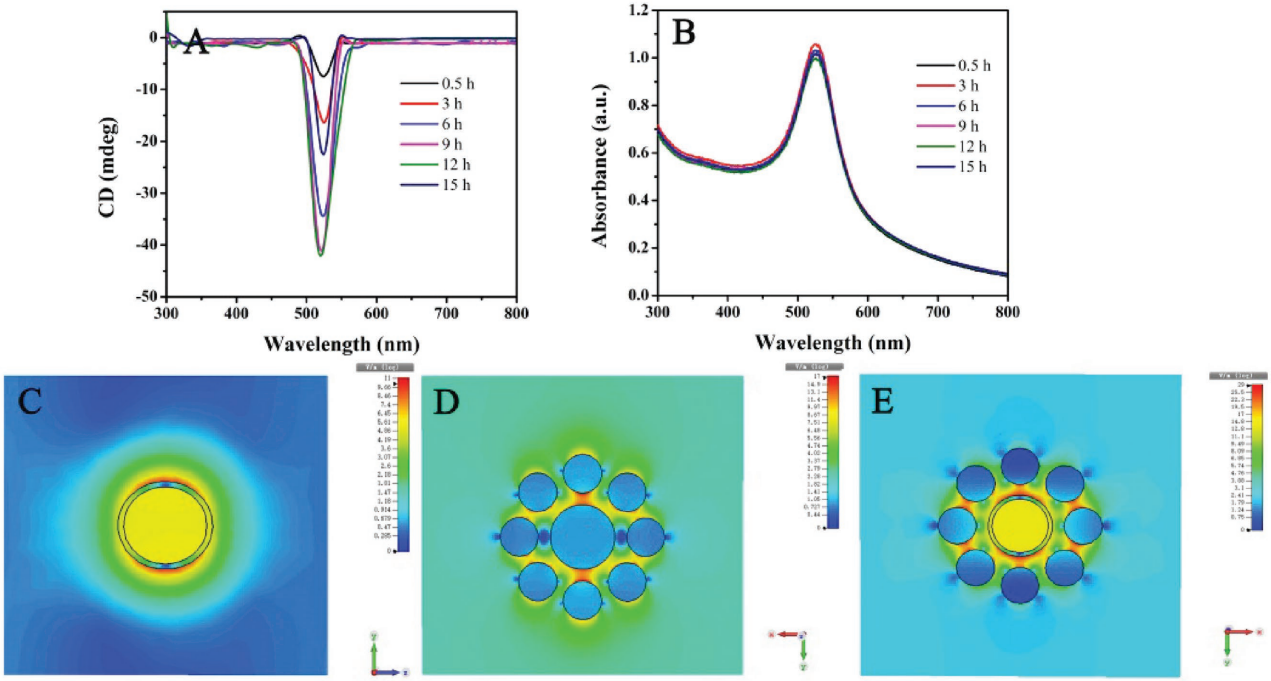

Figure 2. A) CD and B) UV–vis spectra for assembled shell core–Au satellite superstructures at different incubation times. And surface electrical field distribution maps for C) shell NP , D) Au core–Au satellite assembly, and E) shell core–Au satellite assembly, respectively.

and satellite NPs.[45] The asymmetric dipole–dipole interaction between nanoparticles causes the core–satellite structure to produce a strong chiral signal.

In order to verify the special optical characteristics of the assembly structure, we measured the SERS signal of the core–satellite superstructure (Figure S6, Supporting Information); this analysis revealed that the assembly has a relatively strong SERS signal. We attribute the enhancement of the assembly signal to an increase in the number of hot spots between shell and Au NPs.[46] This interpretation is consistent with the results of the CD signal enhancement.

It is worth mentioning that there are several biosensors based on SERS labels embedded core–shell nanostructures.[47,48] These methods utilize SERS properties of the core–shell or shell nanostructure and achieve good detection sensitivity. In this text, a label-free detection method was developed. Compared with other methods, this biosensor has a lower detection limit, which is a more sensitive detection method, indicating that the biosensor has a greater possibility of practical application.

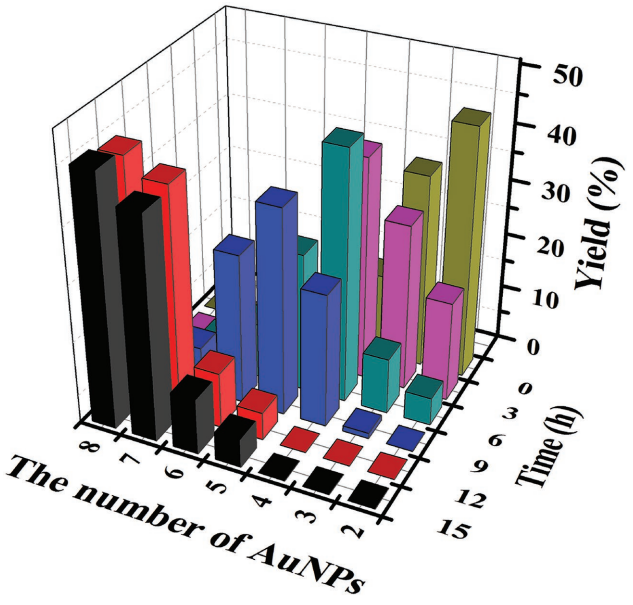

Figure 3. Statistical analysis of the percentage of the number of Au NPs surrounding the shell NPs at different incubation times.

2.2. Construction of the Chiral Sensor for OTA Detection

The OTA detection sensor based on the chiral signal of the core–satellite structure was established and the detection principle of the development strategy is elucidated in Scheme 1. The aptamer-modified shell NPs combined with Au NPs to form a core–satellite structure in the absence of OTA. When OTA was present, it was bound by aptamer, resulting in a decrease in the area that could be conjugated to Au NPs. Correspondingly, the number of Au NPs on the surface of the shell NPs was reduced and the CD signal of the assembly was weakened. We used this feature of the core–satellite superstructure to establish a real-time, sensitive OTA detection chiral sensor.

TEM images, CD, and UV–vis signals were obtained for the core–satellite assembly structure in the presence of different concentrations of OTA (0, 0.1, 0.2, 0.5, 1, 2, and 5 pg mL^{-1}). It can be observed from the TEM images (**Figure 5**A–G) that the number of Au NPs on the surface of the shell NPs decreased

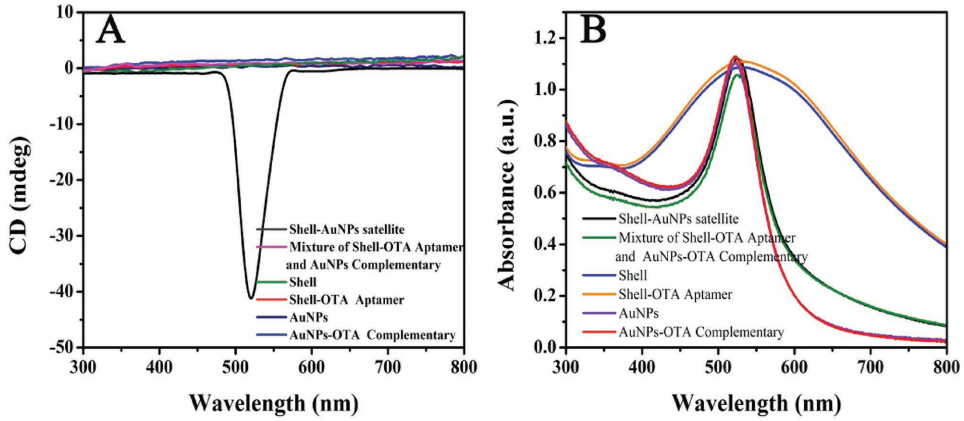

Figure 4. A) CD and B) UV–vis spectra for assembled shell core–Au satellite superstructures and other constituent materials.

with increasing OTA concentration. Correspondingly, the absolute value of the CD signal of the superstructure (**Figure 6**A) also decreased with increasing target concentration. This phenomenon is in line with our expectations. An enlarged view of the core–satellite structure is shown in Figure 5H. There was a good linear relationship of $R^2 = 0.9975$ between the CD signal of the established detection sensor and the concentration of OTA in the range of 0.1–5 pg mL^{-1}, with a limit of detection (LOD) of as low as 0.037 pg mL^{-1} (Figure 6B). Comparison with the literature (Table S1, Supporting Information) shows that the LOD value of the chiral OTA detection sensor based on a core–satellite structure is markedly lower than that of other OTA detection methods. The UV–vis signals of the assembly reactions containing different concentrations of OTA is shown in Figure S7 (Supporting Information).

As a novel biosensor, its stability is an important parameter in practical applications. Here, we investigated the effects of the different salt concentration and the experimental results are shown in Figure S8 (Supporting Information). There was no obvious change in color after addition of 0–30 × 10^{-3} M sodium chloride. However, significant aggregation of the nanostructures occurred after the addition of 40 × 10^{-3} M sodium chloride. To further elucidate the stability, we measured the nanostructured CD signal with addition of 0–30 × 10^{-3} M sodium chloride

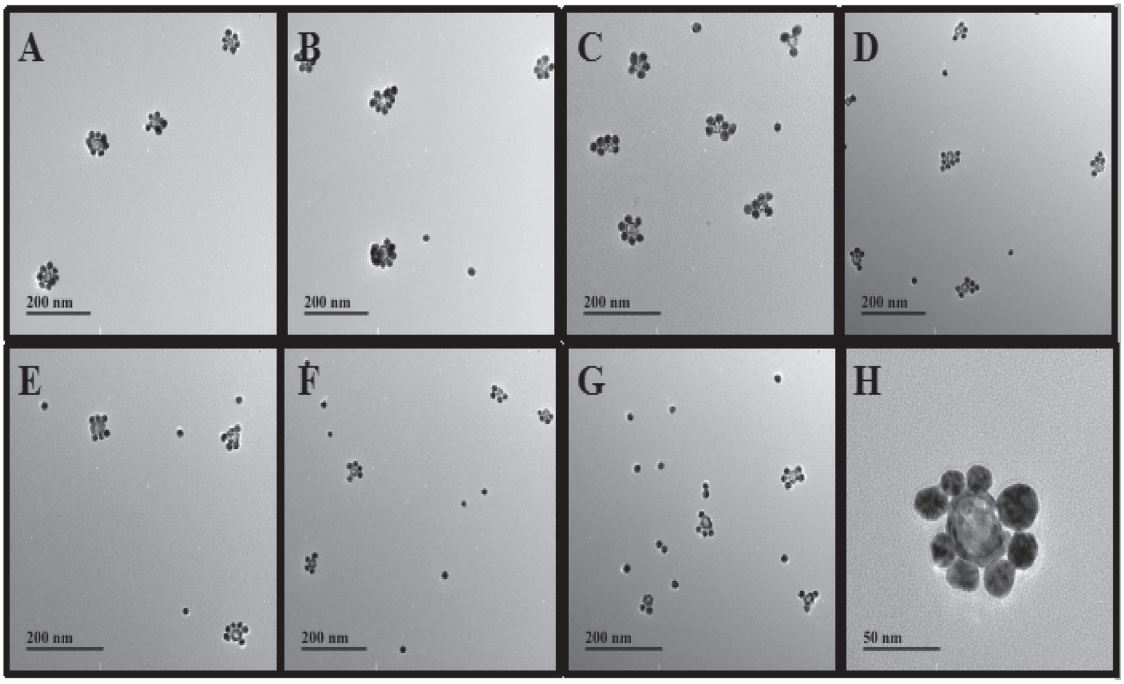

Figure 5. Representative TEM images of shell core–Au satellite superstructures with different assembly levels by adding various concentrations of OTA, A) 0 pg mL^{-1}, B) 0.1 pg mL^{-1}, C) 0.2 pg mL^{-1}, D) 0.5 pg mL^{-1}, E) 1 pg mL^{-1}, F) 2 pg mL^{-1}, and G) 5 pg mL^{-1}, respectively. H) Enlarged image of shell core–Au satellite superstructures.

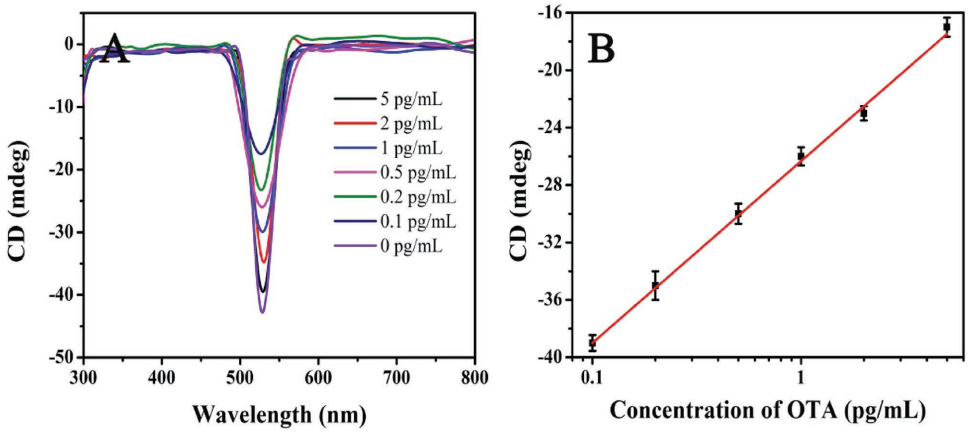

Figure 6. A) CD spectra of shell core–Au satellite superstructures responded to different concentrations of OTA (0, 0.1, 0.2, 0.5, 1, 2, or 5 pg mL^{-1}). B) Plot of CD (521 nm) versus the different concentrations of OTA.

solution. As shown in Figure S8A (Supporting Information), there was no significant change in the CD signal, further demonstrating the stability of the nanostructures.

2.3. Specificity and Selectivity for the OTA Chiral Sensor

In order to verify the specificity and selectivity of the developed OTA sensor assay method, five other mycotoxins, namely ochratoxin B (OTB), fumonisin (FB), aflatoxin M1 (AFM1), aflatoxin B1 (AFB1), and deoxynivalenol (DON) were used. These mycotoxins (all at a concentration of 5 ng mL^{-1}) and OTA (5 pg mL^{-1}) were incubated with DNA-modified NPs, respectively, and a control group without target was included. After 12 h of assembly, the CD signal intensity of the solutions was measured to determine whether the added mycotoxins had an effect on the assembly of the superstructure. The experimental results (**Figure 7**) showed that the CD signal after the addition of the OTA target was significantly lower than the signals obtained after addition of the other targets. Moreover, there was no significant difference between the signal obtained for the other mycotoxin targets and that obtained for the control group, indicating that the OTA chiral sensor has excellent specificity and selectivity among the different mycotoxins. To further confirm the specificity, we increased the amount of above five mycotoxins to 5 ng mL^{-1} and found no response, further confirming the experiment result.

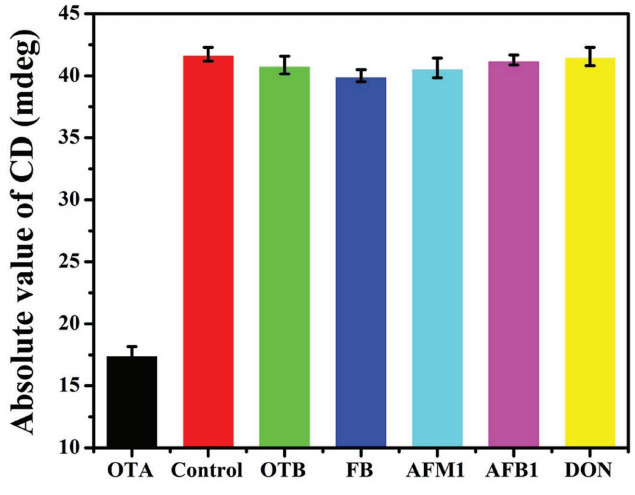

Figure 7. CD intensity (521 nm) of shell core–Au satellite superstructures responded to OTA (5 pg mL^{-1}), OTB (5 ng mL^{-1}), FB (5 ng mL^{-1}), AFM1 (5 ng mL^{-1}), AFB1 (5 ng mL^{-1}), and DON (5 ng mL^{-1}). Control experiment without target was performed.

2.4. Feasibility and Applicability of the OTA Chiral Sensor

To determine the feasibility and applicability of this developed biosensor, the recovery ratio of OTA in red wine samples was analyzed using an addition method. The red wine samples were processed according to a previously described method.[15] Briefly, 0.1, 0.5, or 2 pg mL^{-1} OTA were added to the red wine samples which were validated as OTA-negative using ELISA (Figure S9, Supporting Information). Comparison of the absorbance values of red wine samples at different dilutions with the standard curve of OTA was used to verify that the red wine samples were initially negative for OTA. A satisfactory recovery rate of 96%–104% was achieved (**Table 1**), and at the appropriate sample concentration, the matrix interference was negligible, indicating the practical feasibility of the established detection method.

3. Conclusion

In conclusion, we have here described the development of a DNA-based OTA detection sensor based on core–satellite superstructural chiral signals. The developed strategy can successfully detect OTA in samples in the range of 0.1–5 pg mL^{-1} with an LOD as low as 0.037 pg mL^{-1}. Testing of the sensor with different mycotoxins shows that the sensor possesses excellent selectivity for OTA. Thus, this chiral sensor represents a practical, highly sensitive, highly selective, and real-time OTA residual detection method. It can be used for the testing of

Table 1. Verify the recovery of OTA in the red wine sample.

Sample	Spiked concentration [pg mL^{-1}]	Detected concentration, mean[a)] ± SD[b)] [pg mL^{-1}]	Recovery [%]
Red wine	0.1	0.096 ± 0.0016	96
	0.5	0.518 ± 0.0130	104
	2	1.924 ± 0.0181	96

[a)]The mean of three independent experiments; [b)]SD: Standard deviation.

red wine samples and showed an excellent recovery rate. This method represents a new tool for the detection of low level contamination with residues.

4. Experimental Section

Preparation of Au NPs: Au NPs (15 ± 3 nm) were prepared as described previously.[49] Briefly, 5 mL of a 10×10^{-3} M aqueous $HAuCl_4 \cdot 3H_2O$ solution was mixed with 195 mL deionized (DI) water, and the mixture was heated to boiling. Next, 4.8 mL of a 1% (by weight) sodium citrate solution was added followed by rigorous stirring, and the solution was maintained at boiling temperature for 20 min until the color of the boiling solution changed to a brilliant red. The average particle diameter determined by TEM was 15 ± 3 nm. In order to ensure the stability of Au NPs in high ionic intensity solutions, bis(*p*-sulfonatophenyl)phenylphosphine dihydrate dipotassium salt was incorporated onto the surface of NPs.[50] Finally, Au NPs were concentrated tenfold and stored at 4 °C.

Preparation of Shell NPs. (1) Synthesis of Ag NPs: Ag NPs (25 ± 3 nm) were synthesized according to a previously described method.[51] Briefly, 5 mL poly (*N*-vinyl-2-pyrrolidone (PVP); 1% by weight), 0.6 mL fresh $NaBH_4$ (0.1 M), and 0.6 mL sodium citrate (1% by weight) solution were mixed with 20 mL ice cold water. The mixture was placed in an ice bath and stirred. Then, a solution of 5 mL 1% PVP and 5 mL 10×10^{-3} M $AgNO_3$ solution were simultaneously injected into the previously prepared mixture at a rate of 30 mL h^{-1} using two constant-flow pumps. The reaction solution was kept at 80 °C for 3 h to remove the unreacted $NaBH_4$. The bright yellow solution was cooled to room temperature and then stored at 4 °C.

(2) Synthesis of Shell NPs: Preparation of shell NPs was carried out using a galvanic replacement reaction.[52,53] Typically, 1 mL of the prepared Ag NP solution was concentrated tenfold and resuspended in 10×10^{-3} M tris-HCl buffer with pH 7.4. Excessive Cl^- in the tris-HCl buffer can dissolve AgCl through a coordinated reaction. Therefore, 6 µL of a 10×10^{-3} M $HAuCl_4$ solution and 8 µL of a 10×10^{-3} M ascorbic acid (Vc) solution were added to the Ag NP solution followed by gentle shaking for 10 s. The solution was centrifuged at 7500 rpm for 10 min and the resulting pellets were resuspended in tris-HCl buffer for later use.

Preparation of Single-Stranded DNA-Modified Shell/Au NPs: Single-stranded DNA-modified NPs were prepared with reference to the previous article.[54,55] Specifically, OTA aptamer was added to shell NP solution at a final concentration of 3×10^{-6} M. After 2 h, 1 µL of 5 M NaCl was added dropwise until a final concentration of 0.3 M NaCl was reached. Afterward, the mixture was allowed to stand for 12 h to complete the functionalization of single-stranded DNA. After completion of DNA coupling, the solution was centrifuged at 7500 rpm for 10 min, washed three times, and resuspended in tris-HCl buffer. OTA complementary aptamer was added at a molar ratio of 1:50 to the concentrated Au NPs at a final concentration of 500×10^{-9} M. After that, incubation was carried out at 37 °C for 12 h to complete the coupling. The DNA-functionalized Au NPs were centrifuged at 10 000 rpm for 10 min, washed three times, and dissolved in tris-HCl buffer. Functionalized NPs were then PEGylated with the addition of a 5 kDa poly(ethylene glycol) (PEG) solution to the mixture at a ratio of 1000 PEG molecules per NP in the mixture. PEGylation was performed by incubation at 37 °C for 2 h followed by three washes by centrifugation to remove the excess PEG. After the last wash, NPs were resuspended in tris-HCl buffer.[56]

Preparation of the OTA-Based Chiral Sensor: Shell NP aptamer and the complementary Au NP were combined at a molar ratio of 1:8, thoroughly mixed, and then different concentrations of OTA standard solution (0, 0.1, 0.2, 0.5, 1, 2, 5 pg mL^{-1}) were added to the reaction. The solution was incubated for 12 h at 37 °C for core–satellite assembly.

Determination of OTA in Red Wine Samples: In order to verify the feasibility and applicability of the developed method, we determined the concentration of OTA in samples of red wine. To this end, 0.1 g of PVP was added to 10 mL of OTA-negative red wine samples to remove the precipitate. After filtration, the filtrate was adjusted to pH 7.2 and diluted tenfold for detection.[15] Shell NP aptamer, complementary Au NP, and different concentrations of OTA standard were mixed with the red wine samples, using CD signal for determination.

Supporting Information

Supporting Information is available from the Wiley Online Library or from the author.

Acknowledgements

This work is financially supported by National Key R&D Program (2016YFF0202300), the Natural Science Foundation of Jiangsu Province and MOF (BX20151038, BK20150145, BE2016307), the Self-determined Research Program of Jiangnan University (JUSRP51715A), and Taishan Industry Leading Talent Special Funds.

Conflict of Interest

The authors declare no conflict of interest.

Keywords

biosensors, chiral, nanostructures, ochratoxin A, shell core–satellites, ultrasensitive

Received: November 11, 2017
Revised: January 3, 2018
Published online:

[1] Q. Ying, X. Li, S. Chen, X. P. Zhou, M. Luo, X. Xu, C. R. Li, J. F. Qiu, *Microchim. Acta* **2017**, *184*, 863.
[2] D. Hong, X. Huang, Y. Shao, L. Zheng, G. Liang, Y. Xiong, *Anal. Chem.* **2017**, *89*, 7062.
[3] L. Huang, J. Wu, L. Zheng, H. Qian, F. Xue, Y. Wu, D. Pan, S. B. Adeloju, W. Chen, *Anal. Chem.* **2013**, *85*, 10842.
[4] F. Longobardi, V. Iacovelli, L. Catucci, G. Panzarini, M. Pascale, A. Visconti, A. Agostiano, *J. Agric. Food Chem.* **2013**, *61*, 1604.
[5] X. Liu, Y. Xu, Y. H. Xiong, Z. Tu, Y. P. Li, Z. Y. He, Y. L. Qiu, J. H. Fu, S. J. Gee, B. D. Hammock, *Anal. Chem.* **2014**, *86*, 7471.
[6] A. Breitholtz, M. Olsen, A. Dahlback, K. Hult, *Food Addit. Contam.* **1991**, *8*, 183.
[7] J. Olsson, T. Börjesson, T. Lundstedt, J. Schnürer, *Int. J. Food Microbiol.* **2002**, *72*, 203.
[8] Y. H. Xiong, X. L. Chen, X. U. Yang, *Food Sci.* **2006**, *27*, 30.
[9] L. Liu, L. Xu, S. Suryoprabowo, S. Song, H. Kuang, *Food Agric. Immunol.* **2017**, https://doi.org/10.1080/09540105.2017.1401043.

[10] B. H. Liu, Z. J. Tsao, J. J. Wang, F. Y. Yu, *Anal. Chem.* **2008**, *80*, 7029.
[11] M. Bianco, A. Sonato, A. D. Girolamo, M. Pascale, F. Romanato, R. Rinaldi, V. Arima, *Sens. Actuators, B* **2017**, *241*, 314.
[12] Z. Y. He, Q. H. He, Y. Xu, Y. P. Li, X. Liu, B. Chen, D. Lei, C. H. Sun, *Anal. Chem.* **2013**, *85*, 10304.
[13] L. Rivas, C. C. Mayorgamartinez, D. Quesadagonzález, A. Zamoragálvez, A. D. L. Escosuramuñiz, A. Merkoçi, *Anal. Chem.* **2015**, *87*, 5167.
[14] H. P. Dao, F. Mathieu, A. Lebrihi, *Int. J. Food Microbiol.* **2005**, *104*, 61.
[15] W. Ma, H. Yin, L. Xu, Z. Xu, H. Kuang, L. Wang, C. Xu, *Biosens. Bioelectron.* **2013**, *42*, 545.
[16] G. Whitesides, J. Mathias, C. Seto, *Science* **1991**, *254*, 1312.
[17] C. Lu, Z. Tang, *Adv. Mater.* **2016**, *28*, 1096.
[18] R. Jiang, F. Qin, Y. Liu, X. Y. Ling, J. Guo, M. Tang, S. Cheng, J. Wang, *Adv. Mater.* **2016**, *28*, 6266.
[19] M. Rycenga, C. M. Cobley, J. Zeng, W. Li, C. H. Moran, Q. Zhang, D. Qin, Y. Xia, *Chem. Rev.* **2011**, *111*, 3669.
[20] R. Maoz, E. Frydman, S. R. Cohen, J. Sagiv, *Adv. Mater.* **2000**, *12*, 424.
[21] S. Hamacek, M. Blanc, E. Elhabiri, A. Leize, C. Van Dorsselaer, A. Piguet, M. Albrecht-Gary, *J. Am. Chem. Soc.* **2003**, *125*, 1541.
[22] M. Zhao, F. Yang, C. Liang, D. Wang, D. Ding, J. Lv, J. Zhang, W. Hu, C. Lu, Z. Tang, *Adv. Funct. Mater.* **2016**, *26*, 5182.
[23] Y. Zhou, H. Wang, Y. Zhuo, Y. Chai, R. Yuan, *Anal. Chem.* **2017**, *89*, 3732.
[24] J. Chen, X. Zhang, S. Cai, D. Wu, M. Chen, S. Wang, J. Zhang, *Biosens. Bioelectron.* **2014**, *57*, 226.
[25] C. Wang, J. Qian, K. Wang, K. Wang, Q. Liu, X. Dong, C. Wang, X. Huang, *Biosens. Bioelectron.* **2015**, *68*, 783.
[26] J. Xie, H. Jiang, J. Shen, T. Peng, J. Wang, K. Yao, S. Sun, B. Shao, J. Tang, *Anal. Chem.* **2017**, *89*.
[27] N. L. Rosi, C. A. Mirkin, *Expert Rev. Mol. Diagn.* **2005**, *105*, 1547.
[28] S. W. Thomas, G. D. Joly, T. M. Swager, *Chem. Rev.* **2007**, *107*, 1339.
[29] A. Li, L. Tang, D. Song, S. Song, W. Ma, L. Xu, H. Kuang, X. Wu, L. Liu, X. Chen, C. Xu, *Nanoscale* **2016**, *8*, 1873.
[30] X.-L. Li, S. Liang, F. Nan, Z.-J. Yang, X.-F. Yu, L. Zhou, Z.-H. Hao, Q.-Q. Wang, *Nanoscale.* **2013**, *5*, 5368.
[31] P. Guo, D. Sikdar, X. Huang, K. J. Si, W. Xiong, S. Gong, L. W. Yap, M. Premaratne, W. Cheng, *Nanoscale* **2015**, *7*, 2862.
[32] X. Xu, K. Kim, H. Li, D. L. Fan, *Adv. Mater.* **2012**, *24*, 5457.
[33] L. Xu, C. Hao, H. Yin, L. Liu, W. Ma, L. Wang, H. Kuang, C. Xu, *J. Phys. Chem. Lett.* **2013**, *4*, 2379.
[34] P. Xiaobin, K. Naoki, K. Takahide, O. Atsuhiro, *J. Am. Chem. Soc.* **2007**, *129*, 15947.
[35] A. Nitti, A. Pacini, D. Pasini, *Nanomaterials* **2017**, *7*, 167.
[36] W. Ma, H. Kuang, L. Wang, L. Xu, W. Chang, H. Zhang, M. Sun, Y. Zhu, Y. Zhao, L. Liu, *Sci. Rep.* **2013**, *3*, 1934.
[37] P. Fu, M. Sun, L. Xu, X. Wu, L. Liu, H. Kuang, S. Song, C. Xu, *Nanoscale* **2016**, *8*, 15008.
[38] S. Li, L. Xu, W. Ma, X. Wu, M. Sun, H. Kuang, L. Wang, N. A. Kotov, C. Xu, *J. Am. Chem. Soc.* **2016**, *138*, 306.
[39] X. Wu, L. Xu, W. Ma, L. Liu, H. Kuang, N. A. Kotov, C. Xu, *Adv. Mater.* **2016**, *28*, 5907.
[40] W. Ma, L. Xu, A. F. de Moura, X. Wu, H. Kuang, C. Xu, N. A. Kotov, *Chem. Rev.* **2017**, *117*, 8041.
[41] X. Zhao, X. Wu, L. Xu, W. Ma, H. Kuang, L. Wang, C. Xu, *Biosens. Bioelectron.* **2015**, *66*, 554.
[42] Y. Sun, B. Mayers, Y. Xia, *Adv. Mater.* **2003**, *15*, 641.
[43] W. Ma, H. Kuang, L. Xu, L. Ding, C. Xu, L. Wang, N. A. Kotov, *Nat. Commun.* **2013**, *4*, 2689.
[44] W. Ma, M. Sun, P. Fu, S. Li, L. Xu, H. Kuang, C. Xu, *Adv. Mater.* **2017**, *29*, 1703410.
[45] F. Gao, M. Sun, W. Ma, X. Wu, L. Liu, H. Kuang, C. Xu, *Adv. Mater.* **2017**, *29*, 1606864.
[46] A. X. Wang, X. Kong, *Materials* **2015**, *8*, 3024.
[47] B. Liu, H. Ni, D. Zhang, D. Wang, D. Fu, H. Chen, Z. Gu, X. Zhao, *ACS Sens.* **2017**, *2*, 1035.
[48] Z. Yuan, Y. Yang, Y. Luo, Y. Xuan, M. Li, Q. Song, *ACS Appl. Mater. Interfaces* **2015**, *7*, 21780.
[49] G. Frens, *Nature* **1973**, *241*, 20.
[50] C. J. Loweth, W. B. Caldwell, X. Peng, A. P. Alivisatos, P. G. Schultz, *Angew. Chem., Int. Ed.* **1999**, *38*, 1808.
[51] L. Xu, W. Yan, W. Ma, H. Kuang, X. Wu, L. Liu, Y. Zhao, L. Wang, C. Xu, *Adv. Mater.* **2015**, *27*, 1706.
[52] W. Dehui, X. Xiaohu, W. Yucai, X. Younan, *Small* **2013**, *9*, 3111.
[53] H. Jang, Y. K. Kim, H. Huh, D. H. Min, *ACS Nano* **2014**, *8*, 467.
[54] L. Tang, S. Li, F. Han, L. Liu, L. Xu, W. Ma, K. Hua, A. Li, L. Wang, C. Xu, *Biosens. Bioelectron.* **2015**, *71*, 7.
[55] S. Zhao, W. Ma, L. Xu, X. Wu, H. Kuang, L. Wang, C. Xu, *Biosens. Bioelectron.* **2015**, *68*, 593.
[56] L. Y. Chou, K. Zagorovsky, W. C. Chan, *Nat. Nanotechnol.* **2014**, *9*, 148.